

OctoMag: An Electromagnetic System for 5-DOF Wireless Micromanipulation

Michael P. Kummer, *Student Member, IEEE*, Jake J. Abbott, *Member, IEEE*, Bradley E. Kratochvil, *Member, IEEE*, Ruedi Borer, Ali Sengul, *Student Member, IEEE*, and Bradley J. Nelson, *Senior Member, IEEE*

Abstract—We demonstrate five-degree-of-freedom (5-DOF) wireless magnetic control of a fully untethered microrobot (3-DOF position and 2-DOF pointing orientation). The microrobot can move through a large workspace and is completely unrestrained in the rotation DOF. We accomplish this level of wireless control with an electromagnetic system that we call OctoMag. OctoMag's unique abilities are due to its utilization of complex nonuniform magnetic fields, which capitalizes on a linear representation of the coupled field contributions of multiple soft-magnetic-core electromagnets acting in concert. OctoMag was primarily designed to control intraocular microrobots for delicate retinal procedures, but it also has potential uses in other medical applications or micromanipulation under an optical microscope.

Index Terms—Magnetic, medical, micromanipulator, microrobot, minimally invasive surgery, untethered, wireless.

I. INTRODUCTION

ONE approach to the wireless control of microrobots is through externally applied magnetic fields. These untethered devices can navigate in bodily fluids to enable a number of new minimally invasive therapeutic and diagnostic medical procedures. We are particularly interested in intraocular microrobots, which have the potential to be used in ophthalmic procedures, such as drug delivery and remote sensing [1], [2]. One particularly difficult procedure for vitreoretinal surgeons to perform is retinal-vein cannulation—the injection of a thrombolytic (i.e., clot-busting) drug into a tiny vein—which is at the limits of human capabilities [3]–[5]. A few groups have proposed robot-assisted solutions for vitreoretinal surgery to attenuate the surgeon's hand tremor [6]–[8]. In these proposed robotic solutions, the delicate retina is still at risk from a tool that is capable of exerting large forces.

Manuscript received October 14, 2009; revised April 29, 2010; accepted August 27, 2010. Date of publication October 7, 2010; date of current version December 8, 2010. This paper was recommended for publication by Associate Editor M. Sitti and Editor W. K. Chung upon evaluation of the reviewers' comments. This work was supported by the National Center of Competence in Research Co-Me of the Swiss National Science Foundation.

M. P. Kummer, B. E. Kratochvil, R. Borer, and B. J. Nelson are with the Institute of Robotics and Intelligent Systems, ETH Zurich, 8092 Zurich, Switzerland (e-mail: kummern@ethz.ch; bkratochvil@ethz.ch; rborer@ethz.ch; bnelson@ethz.ch).

J. J. Abbott is with the Department of Mechanical Engineering, University of Utah, Salt Lake City, UT, 84112 USA (e-mail: jake.abbott@utah.edu).

A. Sengul is with the Laboratoire de Systèmes Robotiques, École Polytechnique Fédérale de Lausanne, 1015 Lausanne, Switzerland (e-mail: ali.sengul@epfl.ch).

Color versions of one or more of the figures in this paper are available online at <http://ieeexplore.ieee.org>.

Digital Object Identifier 10.1109/TRO.2010.2073030

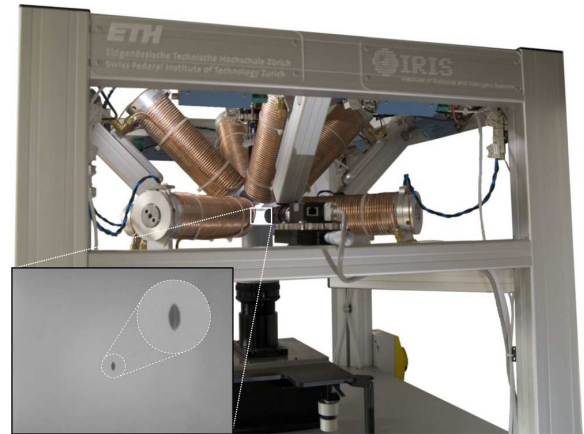


Fig. 1. OctoMag prototype designed and constructed at ETH Zurich. The system contains eight 210-mm-long by 62-mm-diameter electromagnets. The gap between two opposing electromagnets on the lower set is 130 mm. The inset shows a 500- μ m-long microrobot of the type described in [11] levitating in a chamber. This is the side-camera view seen by the operator.

With the goal of enabling less invasive and safer retinal surgery, as well as providing an increased level of dexterity desired by clinicians [9], the task of designing a system for magnetic manipulation of a fully untethered dexterous microrobotic device inside the eye was undertaken. A magnetic device is fundamentally force controlled, with localization required for closed-loop position control, as opposed to manual surgery and existing robotic tools, which are fundamentally position controlled with force sensing or visual feedback of tissue interaction required for closed-loop force control. This makes a magnetic tool a safer device for interacting with the retina: Limits can be imposed on the system to make irreparable retinal damage impossible, even in the event of patient movement or system failure. Ophthalmic procedures are also unique among minimally invasive medical procedures in that they provide a direct line of sight for visual feedback to make closed-loop position control of intraocular microrobots possible [10].

The result of this design effort is an electromagnetic system called OctoMag. The prototype system built is shown in Fig. 1, and a concept image showing how OctoMag would be used for control of intraocular microrobots is shown in Fig. 2. OctoMag enables five-degree-of-freedom (5-DOF) wireless magnetic control of a fully untethered microrobot (3-DOF position and 2-DOF pointing orientation). The microrobot can move through a large workspace and is completely unrestrained in the rotation DOF, which has not been demonstrated previously. Although magnetic manipulation has typically relied on

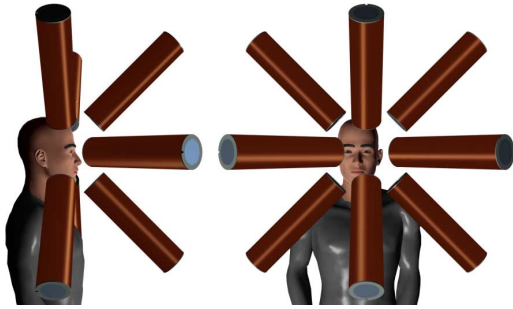


Fig. 2. Concept image of the OctoMag electromagnetic system for the control of intraocular microrobots. An eyeball is at the center of the system's workspace. The electromagnet arrangement accommodates the geometry of the head, neck, and shoulders. The OctoMag is designed for a camera to fit down the central axis to image the microrobot in the eye. Homothetically increasing the size of the prototype system to accommodate a human head will require more powerful current amplifiers to generate the same magnetic field strength. In addition, because the strength of the field gradients attenuates by the same factor by which the system is scaled, the optimal balance of magnetic field and field gradients for a given manipulation task is likely to change, compared with the prototype system.

orthogonal electromagnetic arrangements generating uniform fields and so-called uniform-gradient fields, which are simple in terms of modeling and control, OctoMag's level of wireless control is due to its utilization of complex nonuniform magnetic fields.

There is a large body of prior work discussing wireless manipulation with magnetic fields, using a wide variety of techniques. A significant portion of this paper is aimed at medical applications [12], [13]. Some of the earliest systems were designed to pull a magnetic seed through brain tissue using incremental pulses [14], [15]. There is currently one wireless magnetic system in clinical use: the Stereotaxis Niobe magnetic navigation system, which uses two massive permanent magnets to steer magnetically tipped catheters in the cardiovascular system [16], [17]. The use of position-controlled high-permeability shielding materials to modify the magnetic fields of permanent magnets was proposed as an alternative method to control magnetically tipped catheters, with the potential for smaller and less costly systems [18]. It has been shown that the coils of a clinical MRI system can be used to control untethered magnetic beads in 3-DOF [19]. A variety of swimming magnetic microrobots have been developed nominally for biomedical applications, including helical microrobots inspired by the propulsion of bacterial flagella [20]–[22], microrobots propelled by elastic tails [23], and chains of paramagnetic beads [24] that are inspired by the propulsion of eukaryotic flagella. Researchers have developed a variety of wireless magnetic microrobots that demonstrate impressive performance on planar surfaces but that rely on the planar surface to support the microrobot's weight. These include pulling laterally on the microrobot with magnetic field gradients [11], exciting resonance in the microrobot's structure [25], and creating rocking motions of the microrobot that results in net lateral movement [26], [27]. A number of groups have created electromagnetic systems for 3-DOF manipulation of small magnetic particles in fluid under a microscope [28], [29], and others have demonstrated 3-DOF manipulation of a

microrobot levitated in air [30]. A few magnetic levitation systems have demonstrated 6-DOF controlled movement, but it has always been over a very restricted workspace, particularly in the rotation DOF [31]–[33].

The design of OctoMag began with a few basic goals as follows.

- 1) Stationary electromagnets were chosen for their safety: They do not require moving parts to control field strength, they are inert when powered down, and they are fail-safe, in that the microrobot simply drifts down under its own weight in the event of power failure. Soft-magnetic cores were chosen over air cores because they create a field that is approximately 20 times stronger. As opposed to air-core electromagnets, their individual fields do not linearly superimpose, which complicates modeling and control. However, as we will show, cores made of high-performance soft-magnetic materials impose only a very minor constraint on modeling and control if they are operated within their linear magnetization region, which is sufficiently large based on practical power limits. The use of superconducting electromagnets was precluded, since superconduction would not allow for rapidly varying currents needed for high-bandwidth real-time control.
- 2) Although the required number or configuration of electromagnets was unknown, the resultant design needed to respect the geometry of the human head, neck, and shoulders. Microrobot control has typically relied on systems that fully surround the workspace, such as orthogonal arrangements of electromagnetic coil pairs, which are technically difficult to scale up to the size that would be required for control of *in vivo* devices.
- 3) To validate theoretical results, a prototype system was to be built which was large enough that, after experimenting in artificial and *ex vivo* eyes, could be used for animal trials with live cats and rabbits. This required a usable workspace the size of a 25-mm-diameter sphere, corresponding to the interior volume of a human eye, and it required a larger open volume between the electromagnets to accommodate a small animal head. It was determined that a sphere of diameter 130mm would suffice.
- 4) The workspace should be nearly isotropic, with the ability to generate sufficient magnetic forces in any direction with any microrobot pose. This decision was made because, for the target intraocular-microrobot application, an upward force will be required to levitate the microrobot against its own weight, while downward and lateral forces will be required during retinal procedures.

This open-ended design problem was approached by first solving the control system problem: Given an arbitrary number of stationary electromagnets in an arbitrary configuration, what is a viable control system for 5-DOF control of magnetic microrobots? This is the topic of Section II. Using the final control system, the performance of the resulting system was considered to optimize the design of the electromagnet configuration; this is discussed in Section III. After finalizing the electromagnet configuration, and considering the desired workspace size, the mechatronic components were designed; this is detailed in

Section IV. The system is characterized in Section V. Section VI demonstrates the capabilities of OctoMag in both autonomous and teleoperation control modes. In Section VII, OctoMag is used to control an untethered agent to puncture veins of the vasculature of the chorioallantoic membrane (CAM) of a developing chicken embryo. Finally, some additional potential applications for OctoMag are discussed in Section VIII.

II. CONTROL WITH STATIONARY ELECTROMAGNETS

The goal is to perform 5-DOF wireless control of a magnetic microrobot with respect to a stationary world frame of reference. We assume that the microrobot to be controlled is a magnetized body described by a magnetic moment \mathbf{M} in units ampere meter square. With a permanent magnet, the magnetic moment \mathbf{M} is assumed to have a constant magnitude and be rigidly connected to the frame of the body. With a soft-magnetic body, the magnetic moment is dependent on the applied field and cannot be assumed to be rigidly attached to the body, i.e., the magnetic moment can rotate with respect to the body, and its magnitude can vary greatly with changes in the applied field. In prior work, we have generated accurate models for the field-dependent magnetic moment of axially symmetric bodies [34], which includes ellipsoids and spheres, as well as assembled-microelectromechanical systems (MEMS) structures [35] like those used here.

The torque on the magnet, in newton meters, is expressed as follows:

$$\mathbf{T} = \mathbf{M} \times \mathbf{B} \quad (1)$$

where \mathbf{B} is the value of the applied magnetic field's flux density at the location of \mathbf{M} in teslas [36]. The torque tends to align the magnetic moment with the applied field. In the case of soft-magnetic bodies, the torque tends to align the longest axis of the body (referred to as the easy axis) with the field. If we assume uniform magnetization throughout the body—a reasonable assumption for small elliptical shapes—it is difficult to control torque about the axis of \mathbf{M} using the simple model in (1), which is the reason why our goal is to achieve 5-DOF control rather than 6-DOF control. In soft-magnetic bodies, this means that we are unable to perform rotations about the long axis of the body. To represent vector cross products, the skew-symmetric matrix form of a vector shall be used, i.e., $\mathbf{M} \times \mathbf{B} = \text{Sk}(\mathbf{M})\mathbf{B}$ with

$$\text{Sk}(\mathbf{M}) = \text{Sk}\left(\begin{bmatrix} m_x \\ m_y \\ m_z \end{bmatrix}\right) = \begin{bmatrix} 0 & -m_z & m_y \\ m_z & 0 & -m_x \\ -m_y & m_x & 0 \end{bmatrix} \quad (2)$$

where x , y , and z explicitly refer to the basis directions of the world frame in which all vectors are expressed. The force on the magnetic moment, in newtons, is expressed as follows:

$$\mathbf{F} = (\mathbf{M} \cdot \nabla) \mathbf{B}. \quad (3)$$

Since there is no electric current flowing through the region occupied by the body, Maxwell's equations provide the constraint $\nabla \times \mathbf{B} = \mathbf{0}$. This allows us to express (3), after some

manipulation, in a more intuitive form

$$\mathbf{F} = \left[\frac{\partial \mathbf{B}}{\partial x} \quad \frac{\partial \mathbf{B}}{\partial y} \quad \frac{\partial \mathbf{B}}{\partial z} \right]^T \mathbf{M}. \quad (4)$$

Note that the applied magnetic field can also be described by \mathbf{H} in units ampere per meter with $\mathbf{B} = \mu_0 \mathbf{H}$ and $\mu_0 = 4\pi \times 10^{-7} \text{ T}\cdot\text{m/A}$.

Within a given static arrangement of electromagnets, each electromagnet creates a magnetic field throughout the workspace that can be precomputed. At any given point in the workspace \mathbf{P} , the magnetic field due to actuating a given electromagnet can be expressed by the vector $\mathbf{B}_e(\mathbf{P})$, whose magnitude varies linearly with the current through the electromagnet and, as such, can be described as a unit-current vector in tesla per ampere multiplied by a scalar current value in amperes:

$$\mathbf{B}_e(\mathbf{P}) = \tilde{\mathbf{B}}_e(\mathbf{P})i_e. \quad (5)$$

The subscript e represents the contribution due to actuating the e th electromagnet. However, although the field $\mathbf{B}_e(\mathbf{P})$ is the field due to the current flowing through only electromagnet e , it is due to the soft-magnetic cores of every electromagnet. With air-core electromagnets, the individual field contributions are decoupled, and the fields can be individually precomputed and then linearly superimposed. This is not the case with soft-magnetic-core electromagnets. However, if an ideal soft-magnetic material with negligible hysteresis is assumed, and the system is operated with the cores in their linear magnetization region, the assumption is still valid that the field contributions of the individual currents (each of which affect the magnetization of every core) superimpose linearly. Thus, if the field contribution of a given electromagnet is precomputed *in situ*, it can be assumed that the magnetic field at a point in the workspace is the sum of the contributions of the individual currents

$$\mathbf{B}(\mathbf{P}) = \sum_{e=1}^n \mathbf{B}_e(\mathbf{P}) = \sum_{e=1}^n \tilde{\mathbf{B}}_e(\mathbf{P})i_e. \quad (6)$$

This assumption is clearly also valid for air-core electromagnets. This linear summation of fields can be expressed as follows:

$$\mathbf{B}(\mathbf{P}) = [\tilde{\mathbf{B}}_1(\mathbf{P}) \quad \cdots \quad \tilde{\mathbf{B}}_n(\mathbf{P})] \begin{bmatrix} i_1 \\ \vdots \\ i_n \end{bmatrix} = \mathcal{B}(\mathbf{P})\mathbf{I}. \quad (7)$$

The $3 \times n$ $\mathcal{B}(\mathbf{P})$ matrix is defined at each point \mathbf{P} in the workspace, which can either be analytically calculated online, or a grid of precomputed or measured points can be interpolated online. It is also possible to express the derivative of the field in a given direction in a specific frame, for example, the x -direction, as the contributions from each of the currents

$$\frac{\partial \mathbf{B}(\mathbf{P})}{\partial x} = \left[\frac{\partial \tilde{\mathbf{B}}_1(\mathbf{P})}{\partial x} \quad \cdots \quad \frac{\partial \tilde{\mathbf{B}}_n(\mathbf{P})}{\partial x} \right] \begin{bmatrix} i_1 \\ \vdots \\ i_n \end{bmatrix} = \mathcal{B}_x(\mathbf{P})\mathbf{I}. \quad (8)$$

Considering (1) and (4), the magnetic torque and force on the microrobot can be expressed as follows:

$$\begin{bmatrix} \mathbf{T} \\ \mathbf{F} \end{bmatrix} = \begin{bmatrix} \text{Sk}(\mathbf{M}) \mathcal{B}(\mathbf{P}) \\ \mathbf{M}^T \mathcal{B}_x(\mathbf{P}) \\ \mathbf{M}^T \mathcal{B}_y(\mathbf{P}) \\ \mathbf{M}^T \mathcal{B}_z(\mathbf{P}) \end{bmatrix} \begin{bmatrix} i_1 \\ \vdots \\ i_n \end{bmatrix} = \mathcal{A}_{T,F}(\mathbf{M}, \mathbf{P}) \mathbf{I} \quad (9)$$

i.e., for each microrobot pose, the n electromagnet currents are mapped to a torque and force through a $6 \times n$ actuation matrix $\mathcal{A}_{T,F}(\mathbf{M}, \mathbf{P})$. For a desired torque/force vector, the choice of currents that gets us closest to the desired torque/force value can be found using the pseudoinverse [37]

$$\mathbf{I} = \mathcal{A}_{T,F}(\mathbf{M}, \mathbf{P})^\dagger \begin{bmatrix} \mathbf{T}_{\text{des}} \\ \mathbf{F}_{\text{des}} \end{bmatrix}. \quad (10)$$

The use of (9) requires knowledge of the microrobot's pose and magnetic moment. If there are multiple solutions to achieve the desired torque/force, the pseudoinverse finds the solution that minimizes the two-norm of the current vector, which is desirable for the minimization of both power consumption and heat generation. The pseudoinverse of \mathcal{A} makes use of the singular value decomposition $\mathcal{A} = U\Sigma V^T$, where Σ is the $6 \times n$ singular-value matrix, where the leftmost 6×6 elements form a diagonal matrix of the six-ordered singular values σ_i , U is the 6×6 orthonormal matrix, whose columns are the six output singular vectors, and V is the $n \times n$ orthonormal matrix, whose columns are the n input singular vectors. The pseudoinverse is computed as $\mathcal{A}^\dagger = V\Sigma^\dagger U^T$, where Σ^\dagger is an $n \times 6$ matrix, where the uppermost 6×6 elements form a diagonal matrix with the j th diagonal element defined as $1/\sigma_j$ if $\sigma_j \neq 0$ and as 0 if $\sigma_j = 0$, and all other entries being equal 0 [37]. The sixth singular value will always be $\sigma_6 = 0$ and the sixth column of U will always be

$$U_6 = [0 \ 0 \ 1 \ 0 \ 0 \ 0]^T \quad (11)$$

corresponding to no-torque generation about the magnetization axis, which is never possible. For full 5-DOF control, the other five singular values must be nonzero.

In the case of a microrobot moving through fluid, where the microrobot can align with the applied field unimpeded, a modified control strategy can be applied. Rather than explicitly controlling the torque, one can simply control the magnetic field to the desired orientation, to which the microrobot will naturally align, and then explicitly control the force on the microrobot

$$\begin{bmatrix} \mathbf{B} \\ \mathbf{F} \end{bmatrix} = \begin{bmatrix} \mathcal{B}(\mathbf{P}) \\ \mathbf{M}^T \mathcal{B}_x(\mathbf{P}) \\ \mathbf{M}^T \mathcal{B}_y(\mathbf{P}) \\ \mathbf{M}^T \mathcal{B}_z(\mathbf{P}) \end{bmatrix} \begin{bmatrix} i_1 \\ \vdots \\ i_n \end{bmatrix} = \mathcal{A}_{B,F}(\mathbf{M}, \mathbf{P}) \mathbf{I}. \quad (12)$$

The current \mathbf{I} is then set as follows:

$$\mathbf{I} = \mathcal{A}_{B,F}(\mathbf{M}, \mathbf{P})^\dagger \begin{bmatrix} \mathbf{B}_{\text{des}} \\ \mathbf{F}_{\text{des}} \end{bmatrix}. \quad (13)$$

Full 5-DOF control, which required a rank-5 actuation matrix in (9), corresponds to a rank-6 actuation matrix in (12). As with (9), the use of (12) requires knowledge of the microrobot's pose

and magnetic moment. However, in this case, the microrobot will align with the applied field under open-loop control. If the direction of \mathbf{B} does not change too rapidly, it is reasonable to assume that \mathbf{M} is always aligned with \mathbf{B} , which means that one needs not explicitly measure the microrobot's full pose but, rather, must only estimate the magnitude of \mathbf{M} and measure the microrobot's position \mathbf{P} . In addition, if the magnetic field does not vary greatly across the workspace, it may be reasonable to assume that the microrobot is always located at $\mathbf{P} = \mathbf{0}$ for purposes of control, eliminating the need for any localization of the microrobot. These assumptions are explored in the following.

There are a number of potential methods to generate the unit-current field maps that are required for the proposed control system. One can either explicitly measure the magnetic field of the final constructed system at a grid of points or compute the field values at a grid of points using finite-element-method (FEM) models. In either case, trilinear interpolation is used during real-time control. For each of the electromagnets, a unit-current field map must be calculated. In the event that a given electromagnet configuration exhibits geometrical symmetry, it is possible to calculate fewer maps and then rotate them during run time using homogeneous transformations. To generate the unit-current gradient maps using either method, one can either explicitly measure/model the gradient at the grid of points or numerically differentiate the field data; therefore, special attention must be given to minimize noise in the field map.

An alternative to the trilinear-interpolation approach discussed earlier is to fit a continuous function to the field. This is the approach used in this paper. The analytical field model also has a simple analytical derivative. These analytical models are used to build the unit-current field and gradient maps during run time and are described in more detail in Section V-B.

Throughout this paper, a constant $|\mathbf{B}| = 15$ mT at the location of the microrobot is used: a value chosen after pilot testing because it results in low-peak currents in the electromagnets during typical operation. By keeping $|\mathbf{B}|$ constant, the control system equations are kept linear, which enables (13) to be computed in one iteration, but it is suboptimal. To allow $|\mathbf{B}|$ to vary would result in somewhat better performance but at the added computation cost of optimization in real time.

III. DESIGN OF THE ELECTROMAGNET CONFIGURATION

Once equipped with a general control system using n stationary electromagnets, it is possible to use this controller in the design of the electromagnet configuration. The singular values of the actuation matrix provide information on the condition of the workspace (i.e., points and configurations, where control authority is lost in certain directions). Neither the units for torque and force, nor the units for flux density and force, are the same; therefore, it is difficult to characterize the system with a condition number based on singular values [38]. Considering the practical requirements of the control system, it is more important to accurately control force than torque. Accurate force control will be needed to levitate the microrobot against its own weight in gravity or to push on an object with a specific force. Torque, on the other hand, is only needed to rotate the

microrobot, and a low magnitude of torque applied in the correct direction will ultimately result in the correct control effort, with only the rise time of the controller being affected. The same argument is true for a control system that specifies the magnetic field rather than torque. With this design specification in mind, one can consider a modified actuation matrix, where the field equations are assumed to be attenuated from their true value by some factor $\alpha \ll 1$

$$\begin{bmatrix} \alpha \mathbf{B} \\ \mathbf{F} \end{bmatrix} = \begin{bmatrix} \alpha \mathcal{B}(\mathbf{P}) \\ \mathbf{M}^T \mathcal{B}_x(\mathbf{P}) \\ \mathbf{M}^T \mathcal{B}_y(\mathbf{P}) \\ \mathbf{M}^T \mathcal{B}_z(\mathbf{P}) \end{bmatrix} \begin{bmatrix} i_1 \\ \vdots \\ i_n \end{bmatrix} = \mathcal{A}_m(\mathbf{M}, \mathbf{P}) \mathbf{I}. \quad (14)$$

As $\alpha \rightarrow 0$, the singular values and output singular vectors decouple into pure force and pure-field directions. σ_4 , σ_5 , and σ_6 become small due to α , and the columns U_4 , U_5 , and U_6 tend toward almost pure-field directions. This makes σ_1 , σ_2 , and σ_3 correspond to almost pure-force directions, and the ratio σ_3/σ_1 can be used as a force condition number for the system, which is close to 1 if the system has isotropic force control authority. Keeping $\alpha > 0$ and ensuring that $\sigma_6 \neq 0$ will ensure that the generation of field and, thus, microrobot orientation, is also possible in every desired direction. The force condition number may not be the best metric to judge the system's performance, since a system that has force generation that is equally poor in each direction will return a good force condition number. Consequently, σ_3 , which is a measure of force generation in the worst-case direction, is used as performance metric during design. The goal is to have sufficient force generation capability throughout the workspace, regardless of microrobot orientation, such that control authority of the microrobot is never lost.

To find an electromagnet configuration to achieve the desired performance goals, some design constraints are imposed on the DOF allowed during optimization (see Fig. 3): Two sets of m electromagnets (with $n = 2m$) are considered, which will be referred to as the *upper* and *lower* set, although the goal is a system that has no preferential directions of control, and consequently, no distinction between up and down. Each electromagnet is modeled as a unit-strength point dipole [36] pointing at the common center of the workspace and located at a distance d from the center. The upper and lower sets are organized around a common axis of rotation, with uniform spacing around this axis. The angle between the electromagnets in the upper set and the common axis is defined as ϕ_{upper} , and ϕ_{lower} is defined analogously. Finally, the lower set is allowed to rotate with respect to the upper set by θ .

During optimization, $d = 65$ mm (size requirement for use in trials on small mammals but arbitrary for the design optimization) and $m = \{3, 4\}$ (one at a time) are set as constants. All other parameters are allowed to vary in the bounded sets $\phi_{\text{upper}} \in [0, 90^\circ]$, $\phi_{\text{lower}} \in [0, 180^\circ]$, and $\theta \in [0, 60^\circ]$ when $m = 3$ and $\theta \in [0, 45^\circ]$ when $m = 4$. For a given electromagnet configuration, the point at the common center of the electromagnets, as well as 17 regularly spaced points that define a hemisphere of radius 10 mm are considered. At each of these 18 points, a unit-strength dipole moment (the microrobot) was

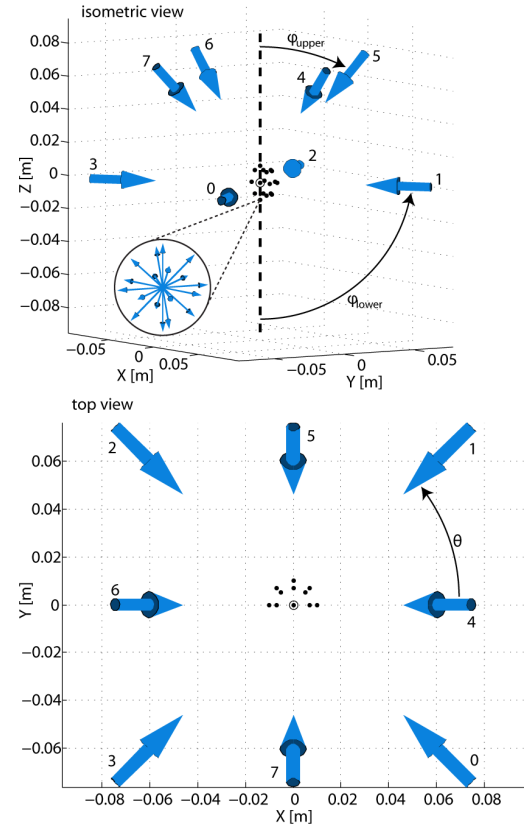


Fig. 3. Optimization of the electromagnet configuration. The upper and lower sets each contain m equally spaced dipoles at an angle ϕ_{upper} and ϕ_{lower} from the common axis, respectively, where $m = 4$ is shown. The dipoles all point at a common center indicated by a circle. The lower set is rotated with respect to the upper set by θ . The 18 microrobot points considered span a hemisphere; each point is indicated by a dot. At each point, 26 microrobot orientations are considered, as shown in the inset. The coil numbering used throughout this paper is shown in both images.

considered at 26 cardinal orientations. The optimization metric for the electromagnet configuration is the lowest (worst case) σ_3 out of the 468 microrobot poses, and the optimization routine (MATLAB's *fmincon*) attempts to maximize this metric. The parameters are allowed to vary without consideration of potential collisions between the electromagnets. For the number of electromagnets, first, $m = 3$ was considered, and afterward, $m = 4$. Although θ was allowed to vary, for an isotropic workspace, from symmetry arguments either $\theta = 0^\circ$ or 60° was expected to be optimal for $m = 3$, and either $\theta = 0^\circ$ or 45° to be optimal for $m = 4$. This procedure was performed for many random combinations of starting values for the three free parameters. The most commonly used configuration of six electromagnets arranged orthogonally and pointing at a common center (e.g., three orthogonal pairs of coils) is a special case allowed by the earlier optimization ($m = 3$, $\theta = 60^\circ$, $\phi_{\text{upper}} = 45^\circ$, and $\phi_{\text{lower}} = 45^\circ$).

The result of the aforementioned optimization routine is the OctoMag configuration shown in Figs. 1–3. We found that, for use with both permanent-magnet and soft-magnetic microrobots, a configuration with $m = 4$, $\theta = 45^\circ$, $\phi_{\text{upper}} \approx 45^\circ$, and $\phi_{\text{lower}} \approx 90^\circ$ resulted in the best performance. System

performance is insensitive to small changes in these nominal values. Although the parameters were allowed to vary with no concern for potential collisions, the optimal configuration is physically realizable. Nearly an order of magnitude improvement was found in the worst-case microrobot pose after increasing from $m = 3$ to 4 (i.e., from six to eight electromagnets). Intuition might lead one to believe that electromagnets must uniformly surround the workspace in order to create an isotropic behavior, but this is not the case. With the OctoMag configuration, pushing downward and pulling upward and sideways can be done, while maintaining any microrobot orientation.

IV. SYSTEM IMPLEMENTATION

Each electromagnet consists of a coil that has dimensions $d_i = 44$ mm, $d_o = 63$ mm, and $l = 210$ mm, where d_i , d_o , and l are inner diameter, outer diameter, and length, respectively. The coil carries 712 wraps of 1.6-mm diameter, insulated copper wire. The electromagnet cores are made of VACOFLUX 50, which is a CoFe alloy from VACUUMSCHMELZE. Its saturation magnetization is on the order of 2.3 T, the coercivity is 0.11 mT, and the maximum permeability is 4500 H/m. The core has diameter 42mm and length 210 mm. The assembled electromagnet has an inductance of 89 mH and a resistance of 1.3 Ω .

The power supply for the system is an SM 70-90 by Delta Elektronika BV. This supply is capable of providing 6 kW to the system and enables all eight channels to be simultaneously driven at 20 A. To reduce the power consumption of the electronics, the current for the electromagnetic coils is sourced through custom-designed switched amplifiers. The switching frequency of these amplifiers is 150 kHz, which is well above the frequency that would influence control of the microrobot. The switched amplifiers are controlled through two Sensoray 626 DAC cards with 14-bit resolution.

In typical operating conditions, the temperature of the coils rises to approximately 60° during a manipulation or characterization task. If the operator wishes to apply the maximum force capable for extended periods of time, the system will rapidly heat up in excess of this. To prevent the temperature in the coils from reaching a critical stage, a cooling system consisting of copper tubing that surrounds each coil has been implemented. While running cooling water through the tubing, temperatures have not exceeded 45° with prolonged application of the maximum current (which rarely occurs in practice).

Two stationary camera assemblies provide visual feedback from the top and side. The cameras (Basler A602fc 60 fps color CMOS firewire cameras) are each fitted with an Edmund Optics VZM 200i 2 \times zoom lens with a working distance of 90 mm a depth-of-field of 1.5 mm and a frame size of 640 \times 480 pixels with an effective pixel size of 19.89 μ m. Each camera assembly is mounted on a Thorlabs DT25/M translation stage, which is used for focusing. Position feedback is achieved with visual processing using the OpenCV library. The simplified experimental environment—a transparent plastic vial—enables successful tracking through the use of adaptive thresholding and morphological operators, such as erosion and dilation. The tracking

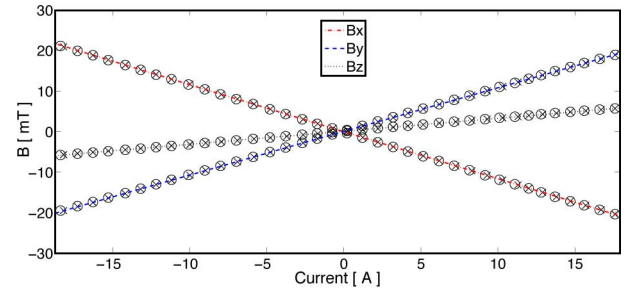


Fig. 4. Hysteresis curve for magnetic field at the center of the workspace as a function of a single coil. \times denotes the data for increasing current, and \circ denotes the data for decreasing current.

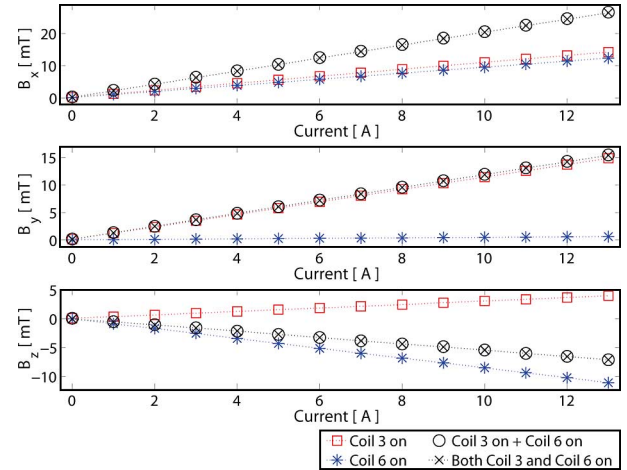


Fig. 5. Verification of system linearity. The field from two coils operating simultaneously is simply the sum of the fields due to the coils individually.

precision is primarily limited by the resolution of the cameras and optics, as discussed in Section VI. The entire system is controlled through C++ by a single computer with an Intel Core 2 Duo 2.6-GHz processor running Ubuntu Linux.

V. SYSTEM CHARACTERIZATION

A. Verification of Linearity Assumption

The concept design of OctoMag is based on the assumption that the use of high-performance soft-magnetic material in the cores will result in a system behavior that is linear with respect to the input currents. The goal is to show that this assumption is indeed valid. Fig. 4 shows the field measured at the center of the workspace as the current is varied in a single electromagnet (Coil 0). The field is measured using a Metrolab THM1176 three-axis Hall magnetometer. We find that there is no perceivable hysteresis below ~ 18 A and that the “linear” region is very linear. In Fig. 5, the field measured at the center of the workspace is shown for the cases, where the current in each of two electromagnets (Coils 3 and 6) is varied individually and then simultaneously. We find that the field generated by both coils is indeed the sum of the fields generated by the individual coils. Recall that the field contribution of a single electromagnet is due to the current through that electromagnet as well as all

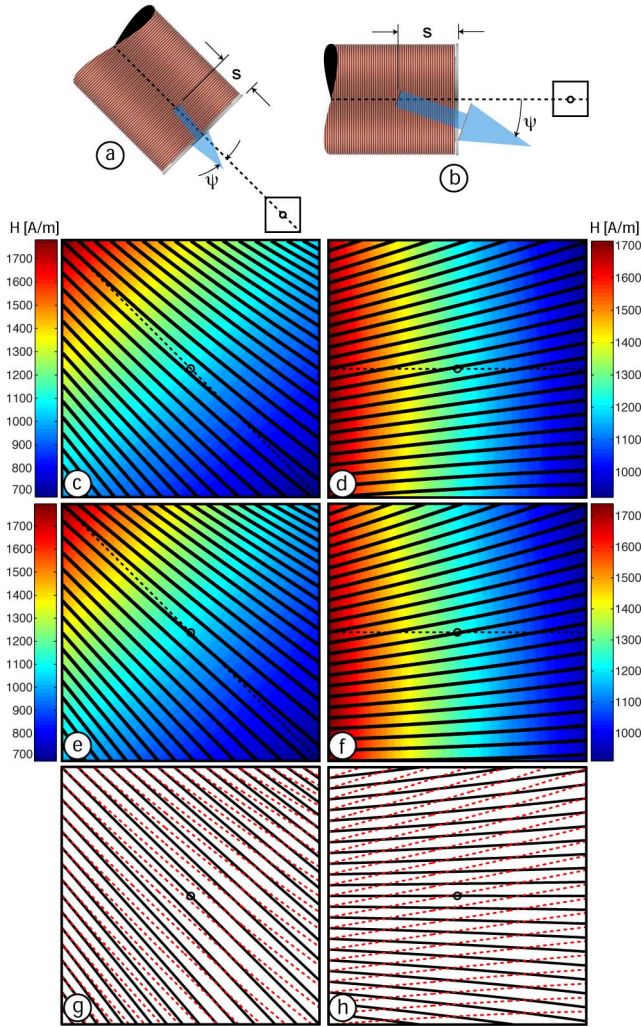


Fig. 6. Fitting a point-dipole model to the FEM simulation for the unit-current field contribution of an upper and lower electromagnet *in situ*. (a) An upper electromagnet is shown on the left, and (b) a lower electromagnet is shown on the right. (c) and (d) FEM data for the central vertical slice within the 20 mm \times 20 mm workspace. (e) and (f) Point-dipole models fit to FEM data along the electromagnet's axis, which is shown with a dotted line. The color gradient represents the magnitude of the magnetic field. The common center of the electromagnets is shown with a circle. It is clear that the other soft-magnetic cores affect the field, as it does not point along the electromagnets axis (c)–(f). For comparison, (g) and (h) show FEM data (red dotted lines) superimposed on the FEM data of an identical, freestanding electromagnet (black solid lines). One can clearly see that the field of a free standing electromagnet does not deflect.

of the soft-magnetic cores. The aforementioned procedure was verified for multiple combinations of coils.

B. Creating the Field Map

As mentioned earlier, to use the control system of Section II, a unit-current field map must be constructed for each of the electromagnets. In this paper, an analytical model—the point-dipole model—was fit to field data obtained from an FEM model of the final system for each of the unit-current contributions. For the cases of an upper and a lower electromagnet, as shown in Fig. 6(a) and (b) and considered separately, the data estimated by the FEM model along the axis of the electromagnet within a

20 mm \times 20 mm vertical, planar region located at the center of the workspace is used. This data is shown in Fig. 6(c) and (d). A point-dipole is fit to this data set using MATLAB's *fmincon* function to minimize the rms error in the fit. The field of a theoretical magnetic point-dipole Γ {A·m²} at each point \mathbf{P} {m} is defined by the relatively simple point-dipole equation [36]

$$\mathbf{B}(\Gamma, \mathbf{P}) = \frac{\mu_0}{4\pi|\mathbf{P}|^3} \left(\frac{3(\Gamma \cdot \mathbf{P})\mathbf{P}}{|\mathbf{P}|^2} - \Gamma \right). \quad (15)$$

During optimization, the point dipole Γ is allowed to translate a distance s along the electromagnet axis, rotate by an angle ψ in the vertical plane (from system symmetry, the dipole should lie in a vertical plane), and change strength. The data for a top and bottom dipole is shown in Fig. 6(e) and (f). For the upper magnet, a point dipole with $|\Gamma| = 4.51 \text{ A}\cdot\text{m}^2$, $s = 22.5 \text{ mm}$, and $\psi = 7.6^\circ$ is computed. For the lower magnet, a point dipole with $|\Gamma| = 8.178 \text{ A}\cdot\text{m}^2$, $s = 34.6 \text{ mm}$, and $\psi = 19.5^\circ$ is computed. Although the model is only fit to data along the electromagnet's axis, it is a sufficient predictor of the field throughout the 20 mm \times 20 mm workspace. To expand to a larger workspace, one could switch to the trilinear-interpolation method discussed in Section II, as it is unlikely that the complex magnetic field of OctoMag can be accurately modeled over a very large workspace using analytical functions.

C. Calibration

To calibrate OctoMag, each of the eight current amplifiers are first calibrated using linear fits. Next, a single-point magnetic-field calibration is performed to compare the actual magnetic field being generated to that predicted by the model utilizing the point-dipole field maps of Section V-B. This calibration is performed to account for imperfections in the magnetic cores, the coil wrapping, and the alignment of the electromagnets. The field is measured at the center of the workspace for 6 A of current flowing through each coil: one at a time. The resultant values are given in Table I, and the errors in magnitude and angle between the two vectors are also given. The error in the amplitude is used as a scaling factor to make the generated field match that computed by the control algorithm, which uses the point-dipole models. The angular error is not compensated for, and it does not change after scaling, but it can be seen that the misalignment between the desired and actual field is small. This calibration provides evidence that rather than having to measure and store unit-current look-up tables for each of the eight electromagnets individually, we may rely on two point-dipole models in the control system. Using the measured calibration values for the respective electromagnet, its field contribution can be calculated through homogeneous transformations of a reference point-dipole model for either an upper or a lower electromagnet.

D. Effect of Position Feedback on Orientation

In some cases, where it is desirable to use OctoMag, computer-vision tracking and localization of the microrobot may be impractical. Fig. 7 shows the microrobot in poses throughout

TABLE I
ONE-POINT CALIBRATION RELATING POINT-DIPOLE MODEL TO FIELD MEASURED AT CENTER OF WORKSPACE FOR 6 A THROUGH A GIVEN COIL

Coil	0	1	2	3	4	5	6	7
$\mathbf{B}_{\text{dipole}}$ (mT)	$\begin{bmatrix} -6.62 \\ 6.62 \\ 1.66 \end{bmatrix}$	$\begin{bmatrix} -6.62 \\ -6.62 \\ 1.66 \end{bmatrix}$	$\begin{bmatrix} 6.62 \\ -6.62 \\ 1.66 \end{bmatrix}$	$\begin{bmatrix} 6.62 \\ 6.62 \\ 1.66 \end{bmatrix}$	$\begin{bmatrix} -6.04 \\ 0.00 \\ -5.29 \end{bmatrix}$	$\begin{bmatrix} 0.00 \\ -6.04 \\ -5.29 \end{bmatrix}$	$\begin{bmatrix} 6.04 \\ 0.00 \\ -5.29 \end{bmatrix}$	$\begin{bmatrix} 0.00 \\ 6.04 \\ -5.29 \end{bmatrix}$
$\mathbf{B}_{\text{measured}}$ (mT)	$\begin{bmatrix} -7.17 \\ 6.76 \\ 2.1 \end{bmatrix}$	$\begin{bmatrix} -6.22 \\ -6.44 \\ 1.19 \end{bmatrix}$	$\begin{bmatrix} 7.02 \\ -6.75 \\ 1.27 \end{bmatrix}$	$\begin{bmatrix} 6.25 \\ 6.55 \\ 1.83 \end{bmatrix}$	$\begin{bmatrix} -4.96 \\ 0.14 \\ -4.36 \end{bmatrix}$	$\begin{bmatrix} -0.07 \\ -5.98 \\ -5.54 \end{bmatrix}$	$\begin{bmatrix} 5.66 \\ 0.34 \\ -4.99 \end{bmatrix}$	$\begin{bmatrix} -0.17 \\ 5.90 \\ -4.73 \end{bmatrix}$
$\frac{ \mathbf{B}_{\text{dipole}} }{ \mathbf{B}_{\text{measured}} }$	0.94	1.05	0.97	1.03	1.22	0.99	1.06	1.06
\angle	2.6°	2.6°	2.8°	1.9°	1.2°	1.7°	2.6°	2.8°

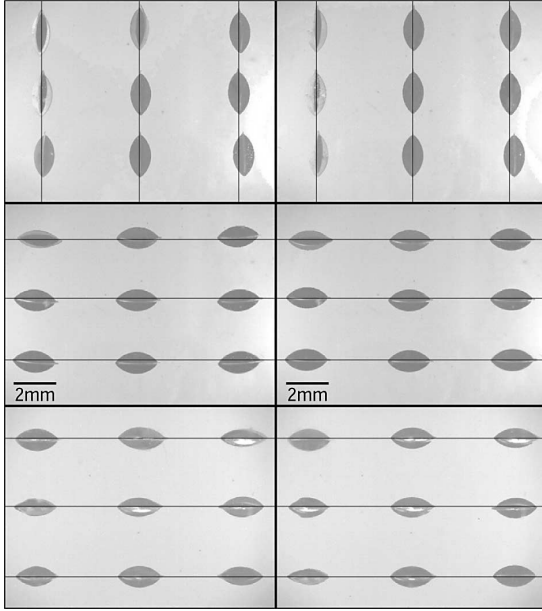


Fig. 7. Composite images showing the effect of position feedback on micro-robot orientation. In each case, the micro-robot is tracked (the computer-vision tracker is not shown for clarity), and the position is used to visually servoed the micro-robot to the desired location for the purpose of taking the photo. Only the images on the right use the position in the computation of the actuation matrix. The images on the left assume that the micro-robot is always located at the center of the workspace. The micro-robot shown is 2 mm long. Row 1: $y = 0$ plane (viewed from the side), micro-robot aligned with X (horizontal). Row 2: $y = 0$ plane, micro-robot aligned with Z (vertical). Row 3: $z = 0$ plane (viewed from above), micro-robot aligned with X (horizontal). The desired orientation of the micro-robot's easy axis is shown with the semitransparent lines in the figures.

the workspace. For the images on the right, the micro-robot is tracked and its true position is used in (12). For the images on the left, the micro-robot is always assumed at the center of the workspace. In most of the poses, it is very difficult to see a significant improvement in orientation with position feedback. This is a consequence of the relative straightness of the field lines in the workspace (see Fig. 6). The primary noticeable change that a user observes when using the system without feedback is an increase in drift at the extremities of the workspace.

E. Force Generation

The maximum force that can be developed with a micro-robot is a function of the size and geometry of the micro-robot.

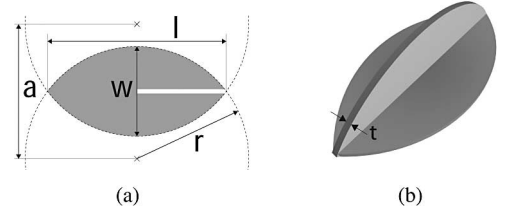


Fig. 8. (a) Microrobots used in this paper are assembled from two electroplated, planar, nearly elliptical pieces, resulting from the intersection of two circles with their centers a distance a apart. The ratio $r/a = 5/6$. A model of an assembled robot can be seen in (b).

TABLE II
EXPERIMENTAL MICROROBOTS: DIMENSIONS AND PROPERTIES

Dimension/ Property	Ni Microrobot	CoNi Microrobot
a (μm)	375	1500
l (μm)	500	2000
w (μm)	250	1000
t (μm)	40	50
volume (m^3)	6.60×10^{-12}	1.37×10^{-10}
density (kg/m^3)	8900	8900
weight (N)	5.76×10^{-7}	1.18×10^{-5}
maximum payload capacity [†] (m^3)	7.39×10^{-12}	7.58×10^{-10}

[†]calculated analogous to [39].

TABLE III
MAX FORCE ON LARGE CO-NI MICROROBOT FOR VARIOUS ORIENTATIONS

Field Orientation	\mathbf{F}_{up} (μN)	\mathbf{F}_{down} (μN)	$\mathbf{F}_{\text{lat},x}$ (μN)	$\mathbf{F}_{\text{lat},y}$ (μN)	$\mathbf{F}_{\text{lat},xy}$ (μN)
z	50.1	39.2	25.1	29.4	35.6
$-z$	83.8	65.8	41.9	49.0	59.3
x	44.6	52.9	50.5	81.3	65.8
xy	65.0	62.3	62.5	67.9	61.7

TABLE IV
MAX FORCE ON SMALL NI MICROROBOT FOR VARIOUS ORIENTATIONS

Field Orientation	\mathbf{F}_{up} (μN)	\mathbf{F}_{down} (μN)	$\mathbf{F}_{\text{lat},x}$ (μN)	$\mathbf{F}_{\text{lat},y}$ (μN)	$\mathbf{F}_{\text{lat},xy}$ (μN)
z	2.46	1.92	1.23	1.44	1.75
$-z$	4.11	3.23	2.06	2.40	2.91
x	2.19	2.59	2.48	3.99	3.23
xy	3.19	3.05	3.06	3.33	3.03

Throughout this paper, we consider two assembled-MEMS microrobots of the type discussed in [11]. The microrobots are assembled from two electroplated, planar pieces shown in Fig. 8. The dimensions and properties of the smaller microrobot made

of Ni and the larger microrobot made of CoNi can be found in Table II. For both microrobots, and for $|\mathbf{B}| = 15$ mT, the maximum magnetic forces that OctoMag can develop in a variety of microrobot configurations are given in Tables III and IV. The values all assume a 15-A saturation of the current amplifiers, using the calibration results of Table I. They also assume the microrobot is at the center of the workspace. For the peripheral workspace points that were considered in the system design, variations in these nominal values ranging from $\sim 0.4\times$ to $\sim 2\times$ have been observed with a minimum and maximum of $\{12.9\ \mu\text{N}, 108\ \mu\text{N}\}$ and $\{0.634\ \mu\text{N}, 5.30\ \mu\text{N}\}$ for the large CoNi and the small Ni microrobot, respectively. Because setting $|\mathbf{B}| = 15$ mT is a suboptimal choice made to linearize the controller, the values given in Tables III and IV represent a lower bound on the true maximum force values. Magnetic force is proportional to volume, if the geometry is held constant. Because the microrobot's weight is also proportional to volume, the ability to levitate a microrobot is unchanged with the microrobot's size. However, because fluid-drag effects are proportional to surface area, a decrease in maximum velocity can be observed as the size of the microrobot is reduced. It is also worth noting that the fluid environment of the microrobot provides a buoyancy force of approximately 14% of the weight.

VI. EXPERIMENTAL DEMONSTRATION

Earnshaw's theorem tells us that there can be no stable static equilibria using ferromagnetism [40], i.e., to maintain a stable position of the microrobot, feedback control must be used. However, once gravity compensation is implemented, we empirically find that the drift of the microrobot in a static field is quite slow. For various microrobot orientations, the worst drift at the center of the workspace in a static field is $150\ \mu\text{m/s}$ for the CoNi microrobot and $50\ \mu\text{m/s}$ for the smaller Ni microrobot. At the boundaries of the workspace, these values increase to 720 and $140\ \mu\text{m/s}$, respectively. Using the microrobot's position for field generation, the drifts at the workspace boundaries reduce to 550 and $60\ \mu\text{m/s}$ for the CoNi and Ni microrobot, respectively. One sees that with scaling the robot down, the effect of drift is reduced—since magnetic forces are proportional to volume, and viscous-drag forces are proportional to surface area—and the behavior and controllability of the microrobot improve. We find that the human operator can regulate the position quite well using only visual feedback, although not with the level of precision as when using the computer-vision tracker for closed-loop control, as described in the following.

We also find that the unintended forces that cause drift are smaller than frictional forces when the microrobot is touching a surface. Even the large microrobot resting on a glass surface exhibits no drift in a static field. Along with the small orientation errors incurred when using no position feedback, which were discussed in Section V-D, this indicates that OctoMag has the potential to be used with no position feedback.

The system is controlled during teleoperation with a 3Dconnexion SpaceExplore 6-DOF elastic rate-control device. The SpaceExplorer lets us exploit the unlimited rotation DOF provided by OctoMag. The SpaceExplorer comes with existing

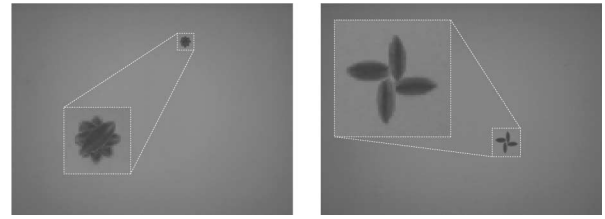


Fig. 9. Demonstration of rotation control. Both time-lapse image sequences show a single $500\text{-}\mu\text{m}$ -long microrobot in the $z = 0$ plane (viewed from above). The left image sequence demonstrates rotation of the microrobot in place at an arbitrary location in space by relying on pure open-loop control. The right image sequence demonstrates rotation of the microrobot about a remote center at an arbitrary location using closed-loop control. Average trajectory-completion time: 5.1 s.

software drivers that allow us to decouple rotation and translation DOF. There is evidence that humans have difficulty conceptualizing rotation and translation simultaneously [41], and we find that decoupling rotation and translation by detecting the user's intended mode does indeed make control more intuitive. We have added an additional mode to decouple movement into individual cardinal directions (in both translation and rotation) and only command the dominant direction being input by the user.

Since the microrobot can be moved from one location to another in a holonomic fashion, closed-loop control of the microrobot is handled by a simple proportional-derivative controller with tracked position from the two cameras. Currently, no closed-loop orientation control is implemented, but as illustrated in Fig. 7, the error between the robots intended orientation and the actual can be accurately controlled open loop, especially if the position is known.

To gauge the precision of the system under closed-loop control, the CoNi microrobot was visually servoed to a location in the center of the workspace. The robot's position, as returned by the tracker, had standard deviations of 6.313 , 4.757 , and $8.951\ \mu\text{m}$ along the x -, y -, and z -axes, respectively, and a maximum Cartesian deviation of $29.77\ \mu\text{m}$ (based on 400 frames collected at 30 Hz).

To further demonstrate the performance of the system under open- and closed-loop control, Figs. 9–12 show a few trajectories of the device, where automated pose control refers to closed-loop position control with open-loop orientation control. The system exhibits similar performance in a wide array of different trajectories as well as for a variety of robot orientations, as illustrated in [42].

VII. In Vitro EXPERIMENT

One targeted medical application of the surgical microrobot is the puncturing of retinal veins to inject thrombolytic drugs or the anchoring of a drug-coated agent for targeted, diffusion-based drug delivery [2]. Leng *et al.* [43] showed that vessels on the CAM of a developing chicken embryo are a valid test bed for studies on human retinal vessel puncture. According to the experimental procedure in [2], a 5-day-old chicken embryo placed in a Petri dish was covered with a layer of AK350 silicon oil to present a clear medium in which an agent could swim. The

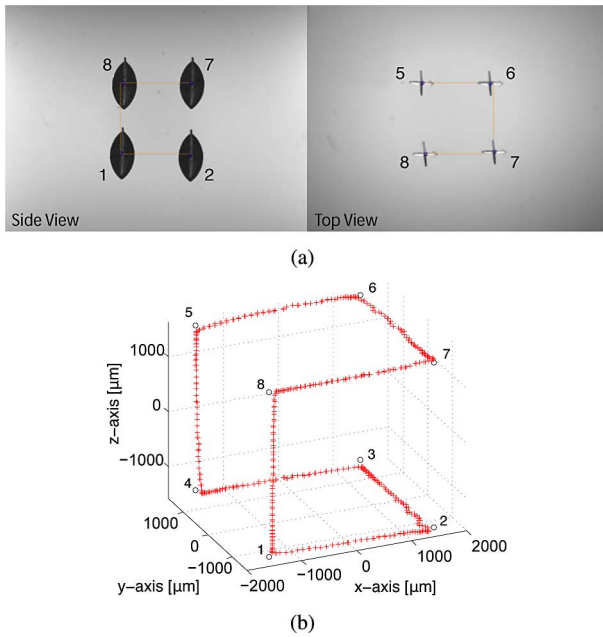


Fig. 10. Demonstration of automated position control. Both composite images (a) show a 2-mm-long microrobot aligned with the Z-axis (vertical). The left image demonstrates movement in the $y = -1.5$ -mm plane. The right image demonstrates movement in the $z = 1.5$ mm plane. Microrobot was moved along the edges of a cube as displayed in the isometric graph (b). Black \circ indicate waypoints and red $+$ indicate tracker data. Average trajectory-completion time: 8.2 s.

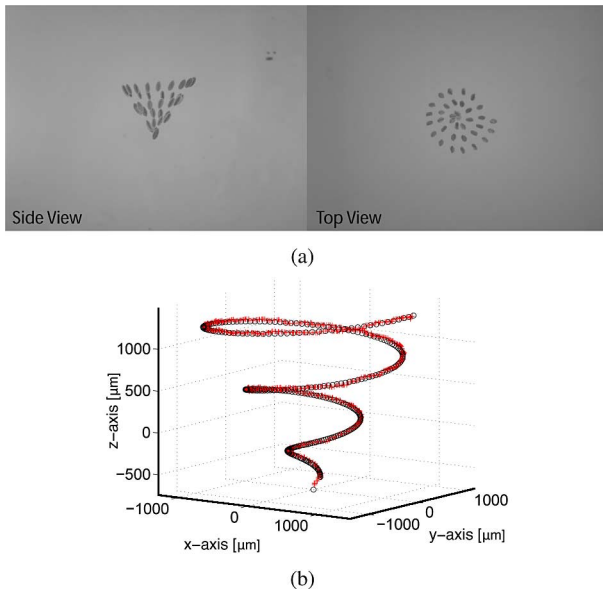


Fig. 11. Demonstration of automated pose control. Both time-lapse image sequences (a) show a 500- μ m-long microrobot following a spiral trajectory keeping its orientation constantly pointing at the vertex of the spiral. Way points (black \circ) and tracker data (red $+$) are shown in the isometric graph (b). Average trajectory-completion time: 33.4 s.

silicon oil layer covered the entire chicken embryo, and the layer stayed on top of the embryo for the duration of the experiment. A puncturing agent consisting of two NdFeB permanent magnet cubes with an 800 μ m (± 100 μ m) cube edge and a ~ 1.2 -mm-long, 30-gauge, glued-on hypodermic needle tip was placed in the silicon oil suspension. The Petri dish was then placed

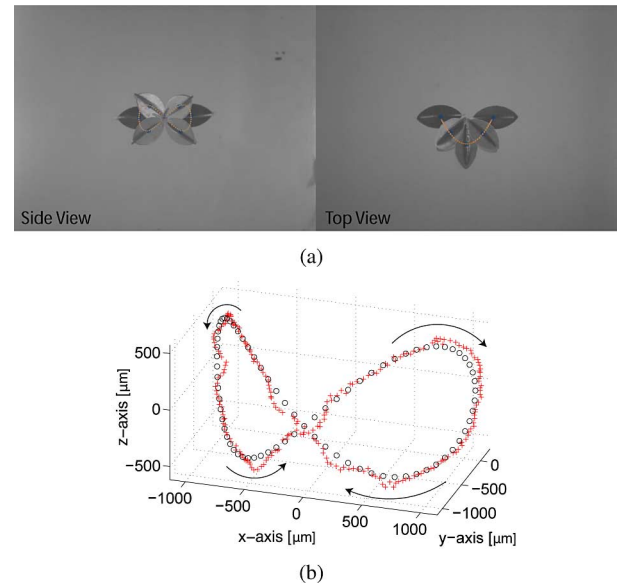


Fig. 12. Demonstration of automated pose control. Both time-lapse image sequences (a) show a 2-mm-long microrobot following a figure-eight trajectory on a spherical surface. The microrobot's orientation is constantly pointing at the center of the sphere. Way points (black \circ) and tracker data (red $+$) are shown in the isometric graph (b). The arrows indicate the direction of motion. Average trajectory-completion time: 8.3 s.

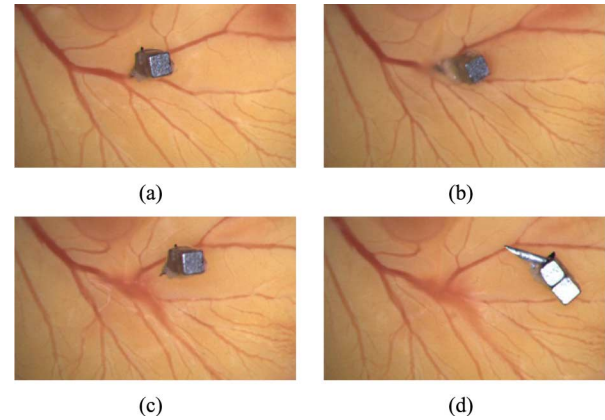


Fig. 13. OctoMag controlling a ~ 2.7 -mm-long NdFeB agent with a hypodermic needle tip to puncture vasculature on a CAM. (a) Taking aim ($t = 9$ s), (b) puncturing ($t = 14$ s), (c) retracting agent ($t = 24$ s), and (d) electromagnets turned off resulting in the agent lying on the CAM ($t = 36$ s).

in the OctoMag setup. Using feedback from the top camera only, it was possible to puncture larger blood vessels (~ 220 μ m outer diameter) of the CAM, as shown in Fig. 13, in a purely open-loop fashion. Using the recorded currents for the puncture experiment in Fig. 13, the force exerted on the CAM at the instance of puncture was calculated to be on the order of 230 μ N when using the relatively large needle tip. An agent of less than half the volume of the agent shown in Fig. 13 would exert the same amount of force if the amplifiers saturate at 15 A. It is also known that smaller, sharper microneedles significantly reduce the force required for puncture [2].

VIII. DISCUSSION

This paper focuses on the use of OctoMag for the control of fully untethered microrobots. OctoMag is also capable of applying controlled magnetic forces and torques in 5-DOF to tethered devices, such as magnetically tipped catheters and guidewires. OctoMag also has potential uses that go beyond medical applications. For example, the OctoMag configuration could be scaled down and used to control microdevices under a light microscope. Since the workspace is designed to be isotropic, OctoMag can be operated upside down or on its side. OctoMag can also be used to control magnetic microrobots that were originally designed to be controlled with uniform magnetic fields. Consider, for example, microscopic helical swimmers designed to be controlled by a rotating uniform magnetic field [22]. With OctoMag, the field can be set to any desired value while setting $\mathbf{F} = \mathbf{0}$ to generate a uniform field. However, if magnetic force is applied to the microrobot as it is rotated, the magnetic force will sum with the fluidic propulsive force, resulting in higher manipulation forces. Considering the desirable propulsive properties of helical magnetic swimmers as they are scaled down [44], this may actually result in larger useful pushing force than is possible with the type of microrobots shown in this paper.

In order to use OctoMag for the control of intraocular microrobots, we must still determine for which vitreoretinal procedures an untethered microrobot is appropriate. Microrobots can clearly be used for remote sensing applications, as well as for targeted delivery of small quantities of concentrated drug. There are two potential drawbacks of magnetic microrobots: their limited ability to apply large forces and their limited ability to carry large payloads. For surgical tasks that require relatively large forces, a microrobot may not be the best choice.

IX. CONCLUSION

We presented 5-DOF wireless magnetic control of a fully untethered microrobot using an electromagnetic system called OctoMag. The system provides precise positioning under closed-loop control with computer vision but can also be used with no visual tracking, relying only on visual feedback to the human operator during direct teleoperation. OctoMag was designed for the control of intraocular microrobots for minimally invasive retinal therapy and diagnosis, but it also has potential for use as a wireless micromanipulation system under a light microscope. As proof of concept, OctoMag was used to perform wireless vessel puncture of CAM blood vessels in an *in vitro* chicken embryo.

ACKNOWLEDGMENT

The authors would like to thank Dr. K. Vollmers for many fruitful discussions in the early stages of the OctoMag project. They would also like to thank O. Ergeneman for assistance with the preparation of the chicken embryos. Finally, they would also like to thank J. Garweg, M.D. from the Swiss Eye Institute in Bern, Switzerland, and C. Framme, M.D., of the Inselspital Bern for their guidance on vitreoretinal applications for untethered microrobots.

REFERENCES

- [1] O. Ergeneman, G. Dogangil, M. P. Kummer, J. J. Abbott, M. K. Nazeeruddin, and B. J. Nelson, "A magnetically controlled wireless optical oxygen sensor for intraocular measurements," *IEEE Sensors J.*, vol. 8, no. 1, pp. 29–37, Jan. 2008.
- [2] G. Dogangil, O. Ergeneman, J. J. Abbott, S. Pane, H. Hall, S. Muntwyler, and B. J. Nelson, "Toward targeted retinal drug delivery with wireless microrobots," in *Proc. IEEE/RSJ Int. Conf. Intell. Robots Syst.*, 2008, pp. 1921–1926.
- [3] P. K. Gupta, P. S. Jensen, and E. de Juan, Jr., "Surgical forces and tactile perception during retinal microsurgery," in *Proc. Int. Conf. Med. Image Comput. Comput.-Assist. Interv.*, 1999, pp. 1218–1225.
- [4] S. P. N. Singh and C. N. Riviere, "Physiological tremor amplitude during retinal microsurgery," in *Proc. IEEE Northeast Bioeng. Conf.*, 2002, pp. 171–172.
- [5] A. D. Jagtap and C. N. Riviere, "Applied force during vitreoretinal microsurgery with handheld instruments," in *Proc. IEEE Int. Conf. Eng. Med. Biol. Soc.*, 2004, pp. 2771–2773.
- [6] C. N. Riviere, W. T. Ang, and P. K. Khosla, "Toward active tremor canceling in handheld microsurgical instruments," *IEEE Trans. Robot. Autom.*, vol. 19, no. 5, pp. 793–800, Oct. 2003.
- [7] B. Mitchell, J. Koo, I. Iorachita, P. Kazanides, A. Kapoor, J. Handa, G. Hager, and R. Taylor, "Development and application of a new steady-hand manipulator for retinal surgery," in *Proc. IEEE Int. Conf. Robot. Autom.*, 2007, pp. 623–629.
- [8] W. Wei, R. E. Goldman, H. F. Fine, S. Chang, and N. Simaan, "Performance evaluation for multi-arm manipulation of hollow suspended organs," *IEEE Trans. Robot.*, vol. 25, no. 1, pp. 147–157, Feb. 2009.
- [9] S. Charles, "Dexterity enhancement for surgery," in *Computer Integrated Surgery: Technology and Clinical Application*, R. H. Taylor, S. Lavallée, G. C. Burdea, and R. Mösges, Eds. Cambridge, MA: MIT Press, 1996, pp. 467–471.
- [10] C. Bergeles, K. Shamaei, J. J. Abbott, and B. J. Nelson, "Single-camera focus-based localization of intraocular devices," *IEEE Trans. Biomed. Eng.*, vol. 57, no. 8, pp. 2064–2074, Aug. 2010.
- [11] K. B. Yesin, K. Vollmers, and B. J. Nelson, "Modeling and control of untethered biomicrobots in a fluidic environment using electromagnetic fields," *Int. J. Robot. Res.*, vol. 25, no. 5–6, pp. 527–536, 2006.
- [12] D. B. Montgomery and R. J. Weggel, "Magnetic forces for medical applications," *J. Appl. Phys.*, vol. 40, no. 3, pp. 1039–1041, 1969.
- [13] G. T. Gillies, R. C. Ritter, W. C. Broadus, M. S. Grady, and M. A. Howard, III, R. G. McNeil, "Magnetic manipulation instrumentation for medical physics research," *Rev. Sci. Instrum.*, vol. 65, no. 3, pp. 533–562, 1994.
- [14] R. G. McNeil, R. C. Ritter, B. Wang, M. A. Lawson, G. T. Gillies, K. G. Wika, E. G. Quate, M. A. Howard, III, and M. S. Grady, "Functional design features and initial performance characteristics of a magnetic-implant guidance system for stereotactic neurosurgery," *IEEE Trans. Biomed. Eng.*, vol. 42, no. 8, pp. 793–801, Aug. 1995.
- [15] D. C. Meeker, E. H. Maslen, R. C. Ritter, and F. M. Creighton, "Optimal realization of arbitrary forces in a magnetic stereotaxis system," *IEEE Trans. Magn.*, vol. 32, no. 2, pp. 320–328, Mar. 1996.
- [16] *Stereotaxis Niobe Magnetic Navigation System*. (2010). [Online]. Available: <http://www.stereotaxis.com>
- [17] I. Tunay, "Modeling magnetic catheters in external fields," in *Proc. IEEE Int. Conf. Eng. Med. Biol. Soc.*, 2004, pp. 2006–2009.
- [18] R. D. Brewer, K. E. Loewke, E. F. Duval, and J. K. Salisbury, "Force control of a permanent magnet for minimally-invasive procedures," in *Proc. IEEE Int. Conf. Biomed. Robot. Biomechanics*, 2008, pp. 580–586.
- [19] S. Martel, J.-B. Mathieu, O. Felfoul, A. Chanu, E. Aboussouan, S. Tamaz, and P. Pouponneau, "Automatic navigation of an untethered device in the artery of a living animal using a conventional clinical magnetic resonance imaging system," *Appl. Phys. Lett.*, vol. 90, no. 114105, 2007.
- [20] T. Honda, K. I. Arai, and K. Ishiyama, "Micro swimming mechanisms propelled by external magnetic fields," *IEEE Trans. Magn.*, vol. 32, no. 5, pp. 5085–5087, Sep. 1996.
- [21] K. Ishiyama, K. I. Arai, M. Sendoh, and A. Yamazaki, "Spiral-type micro-machine for medical applications," *J. Micromechatronics*, vol. 2, no. 1, pp. 77–86, 2003.
- [22] L. Zhang, J. J. Abbott, L. X. Dong, B. E. Kratochvil, D. Bell, and B. J. Nelson, "Artificial bacterial flagella: Fabrication and magnetic control," *Appl. Phys. Lett.*, vol. 94, pp. 064107-1–064107-3, 2009.

- [23] S. Sudo, S. Segawa, and T. Honda, "Magnetic swimming mechanism in a viscous liquid," *J. Intell. Mater. Syst. Struct.*, vol. 17, pp. 729–736, 2006.
- [24] R. Dreyfus, J. Baudry, M. L. Roper, M. Fermigier, H. A. Stone, and J. Bibette, "Microscopic artificial swimmers," *Nature*, vol. 437, no. 6, pp. 862–865, 2005.
- [25] K. Vollmers, D. R. Frutiger, B. E. Kratochvil, and B. J. Nelson, "Wireless resonant magnetic microactuator for untethered mobile microrobots," *Appl. Phys. Lett.*, vol. 92, pp. 144103-1–144103-3, 2008.
- [26] M. Gauthier and E. Piat, "An electromagnetic micromanipulation systems for single-cell manipulation," *J. Micromechatronics*, vol. 2, no. 2, pp. 87–119, 2004.
- [27] C. Pawashe, S. Floyd, and M. Sitti, "Modeling and experimental characterization of an untethered magnetic micro-robot," *Int. J. Robot. Res.*, vol. 28, no. 4, pp. 1077–1094, 2009.
- [28] F. Amblard, B. Yurke, A. Pargellis, and S. Leibler, "A magnetic manipulator for studying local rheology and micromechanical properties of biological systems," *Rev. Sci. Instrum.*, vol. 67, no. 3, pp. 818–827, 1996.
- [29] C. Gosse and V. Croquette, "Magnetic tweezers: Micromanipulation and force measurement at the molecular level," *Biophys. J.*, vol. 82, pp. 3314–3329, 2002.
- [30] M. B. Khamesee, N. Kato, Y. Nomura, and T. Nakamura, "Design and control of a microrobotic system using magnetic levitation," *IEEE/ASME Trans. Mechatronics*, vol. 7, no. 1, pp. 1–14, Mar. 2002.
- [31] S. Verma, W.-J. Kim, and J. Gu, "Six-axis nanopositioning device with precision magnetic levitation technology," *IEEE/ASME Trans. Mechatronics*, vol. 9, no. 2, pp. 384–391, Jun. 2004.
- [32] Z. Zhang and C.-H. Menq, "Six-axis magnetic levitation and motion control," *IEEE Trans. Robot.*, vol. 23, no. 2, pp. 196–205, Apr. 2007.
- [33] P. J. Berkelman and R. L. Hollis, "Lorentz magnetic levitation for haptic interaction: Device design, performance, and integration with physical simulations," *Int. J. Robot. Res.*, vol. 19, no. 7, pp. 644–667, 2000.
- [34] J. J. Abbott, O. Ergeneman, M. P. Kummer, A. M. Hirt, and B. J. Nelson, "Modeling magnetic torque and force for controlled manipulation of soft-magnetic bodies," *IEEE Trans. Robot.*, vol. 23, no. 6, pp. 1247–1252, Dec. 2007.
- [35] Z. Nagy, O. Ergeneman, J. J. Abbott, M. Hutter, A. M. Hirt, and B. J. Nelson, "Modeling assembled-MEMS microrobots for wireless magnetic control," in *Proc. IEEE Int. Conf. Robot. Autom.*, 2008, pp. 874–879.
- [36] E. P. Furlani, *Permanent Magnet and Electromechanical Devices*. San Diego, CA: Academic, 2001.
- [37] R. A. Horn and C. R. Johnson, *Matrix Analysis*. Cambridge, U.K.: Cambridge Univ. Press, 1985.
- [38] K. L. Doty, C. Melchiorri, E. M. Schwartz, and C. Bonivento, "Robot manipulability," *IEEE Trans. Robot. Autom.*, vol. 11, no. 3, pp. 462–468, Jun. 1995.
- [39] O. Ergeneman, J. J. Abbott, G. Dogangil, and B. J. Nelson, "Functionalizing intraocular microrobots with surface coatings," in *Proc. IEEE Int. Conf. Biom. Robot. Biomechatronics*, 2008, pp. 232–237.
- [40] B. D. Cullity and C. D. Graham, *Introduction to Magnetic Materials*, 2nd ed. Hoboken, NJ: Wiley, 2009.
- [41] M. R. Masliah and P. Milgram, "Measuring the allocation of control in a 6 degree-of-freedom docking experiment," in *Proc. SIGCHI Conf. Hum. Factors Comput. Syst.*, New York: ACM, 2000, pp. 25–32.
- [42] B. E. Kratochvil, M. P. Kummer, J. J. Abbott, R. Borer, O. Ergeneman, and B. J. Nelson, "Octomag: An electromagnetic system for 5-DOF wireless manipulation - video submission," presented at the IEEE Int. Conf. Robot. Autom., Anchorage, AK, May 2010.
- [43] T. Leng, J. M. Miller, K. V. Bilbao, D. V. Palanker, P. Huie, and M. S. Blumenkranz, "The chick chorioallantoic membrane as a model tissue for surgical retinal research and simulation," *Retina*, vol. 24, no. 3, pp. 427–434, Jun. 2004.
- [44] J. J. Abbott, K. E. Peyer, M. Cosentino Lagomarsino, L. Zhang, L. X. Dong, I. K. Kaliakatos, and B. J. Nelson, "How should microrobots swim?" *Int. J. Robot. Res.*, vol. 28, no. 11–12, pp. 1434–1447, 2009.



Michael P. Kummer (S'10) received the Diploma degree in mechanical engineering from ETH Zurich, Zurich, Switzerland, in 2005, where he is currently working toward the Ph.D. degree with the Institute of Robotics and Intelligent Systems and is investigating magnetic control of intraocular microrobots.



Jake J. Abbott (M'05) received the Ph.D. degree in mechanical engineering from Johns Hopkins University, Baltimore, MD, in 2005.

In 2005, he became a Postdoctoral Research Associate with the Institute of Robotics and Intelligent Systems, ETH Zurich, Zurich, Switzerland. In 2008, he became an Assistant Professor with the University of Utah, Salt Lake City, where he is currently the Head of the Telerobotics Laboratory, Department of Mechanical Engineering. His research interests include medical and microscale telerobotics.



Bradley E. Kratochvil (M'08) received the Ph.D. degree from ETH Zurich, Zurich, Switzerland, in 2008.

He is currently a Postdoctoral Associate with the Institute of Robotics and Intelligent Systems, ETH Zurich. His research interests include micro/nanomanipulation, computer vision for microscopy, and untethered mobile microrobots.

Dr. Kratochvil was the recipient of Swiss Society for Optics and Microscopy prize for his doctoral work. In 2007 and 2009, he was the Co-Leader of a team that was engaged in the RoboCup Nanogram competition for untethered mobile microrobots.



Ruedi Borer received the Dipl. HTL degree in electro engineering from the University of Applied Science, Zurich, Switzerland, in 1984.

In 1981, he joined Prof. G. Schweitzer at the Institute of Mechanics, ETH Zurich, as an Electronic Technician, where he became a Member of the Institute of Robotics and was engaged in various support and planning tasks. He was a Founder of the new Institute of Robotics and Intelligent Systems, ETH Zurich, in 2002. His current research interests include planning and developing special hardware for research and education.



Ali Sengul (S'10) received the M.S. degree in mechanical engineering from ETH Zurich, Zurich, Switzerland, in 2008. He is currently working toward the Ph.D. degree with the Laboratoire de Systèmes Robotiques, École Polytechnique Fédérale de Lausanne, Lausanne, Switzerland.

His current research interests include modular robots for use in the gastrointestinal tract.



Bradley J. Nelson (SM'06) received the Ph.D. degree in robotics from Carnegie Mellon University, Pittsburgh, PA, in 1995.

In 1995, he became an Assistant Professor with the University of Illinois, Chicago, and an Associate Professor with the University of Minnesota, Minneapolis, in 1998. In 2002, he was a Professor of Robotics and Intelligent Systems, ETH Zurich, Zurich, Switzerland, where he is currently the Head of the Multiscale Robotics Laboratory, as well as the Chairman of the ETH Electron Microscopy Center.

His research interests include microrobotics and nanorobotics.

Dr. Nelson was named to the 2005 Scientific American 50. His laboratory won the biennial RoboCup Nanogram competition in 2007 and 2009. He is also the recipient of multiple best conference paper awards.